



## Facile synthesis of SnSe–MnTe nanocomposite as a promising electrode for supercapacitor applications

Abdul Khalil<sup>a,\*</sup>, Meznah M. Alanazi<sup>b</sup>, Shaimaa A.M. Abdelmohsen<sup>b</sup>, Saeed D. Alahmari<sup>c</sup>, Khalid I. Hussein<sup>d</sup>, A.M.A. Henaish<sup>e,f</sup>, Muhammad Abdullah<sup>g</sup>

<sup>a</sup> Institute of Physics, Gomal University, Dera Ismail Khan, KPK, Pakistan

<sup>b</sup> Department of Physics, College of Science, Princess Nourah bint Abdulrahman University, P.O. Box 84428, Riyadh, 11671, Saudi Arabia

<sup>c</sup> Department of Chemistry, Faculty of Science, Jazan University, P.O. Box 2097, 45142 Jazan, Saudi Arabia

<sup>d</sup> Department of Radiological Sciences, College of Applied Medical Sciences, King Khalid University, Abha 61421, Saudi Arabia

<sup>e</sup> Physics Department, Faculty of Science, Tanta University, Tanta 31527, Egypt

<sup>f</sup> NANOTECH Center, Ural Federal University, Ekaterinburg 620002, Russia

<sup>g</sup> Department of Chemistry, Government College University Lahore, Lahore-54000, Pakistan

### ARTICLE INFO

#### Keywords:

Tin selenide  
Manganese telluride  
Supercapacitor  
Sonication technique  
Energy storage devices

### ABSTRACT

The biggest problems encountered by the world right now are energy demand and environmental damage because of the exploitation of fossil fuels. Producing and storing energy in an environment-friendly way is increasingly crucial due to the exhaustion of non-renewable resources. Developing a robust energy storing system is essential for efficient energy storage, specifically for renewable energy sources. In this study, tin selenide and manganese telluride (SnSe–MnTe) nanocomposite was synthesized via a sonication method for supercapacitor application. Different physical techniques confirmed the enhanced structural and morphological attributes observed for the SnSe–MnTe nanocomposite. During electrochemical investigations, the SnSe–MnTe nanocomposite exhibited specific capacitance, specific energy ( $S_E$ ) and specific power ( $S_P$ ) of 1502 F/g, 61.05 Wh/kg and 270.5 W/kg at 1.0 A/g, correspondingly. Furthermore, it exhibited outstanding cyclic stability, maintaining its performance across 5000th cycles in an electrolyte (2.0 M KOH). Compared to SnSe (1.25  $\Omega$ ) and MnTe (0.69  $\Omega$ ), the charge transfer resistance ( $R_{ct}$ ) value for SnSe–MnTe (0.3  $\Omega$ ) was smaller calculated via Nyquist plot. Therefore, transition metal chalcogenide-based nanocomposite has an excellent potential as electrode material for supercapacitor ( $SC_s$ ) and it can also be utilized in different energy storage devices.

### 1. Introduction

The current global energy issues are directly attributable to the combustion of fossil fuels in large quantities, their supplies become depleted, which could have an impact on the advancement of human civilization, which pollutes the air through the release of greenhouse gases [1]. Regenerative energy sources such as wind energy and solar have outstanding potential but they depend on the weather and hence are unreliable [2,3]. Energy storing devices ( $ESD_s$ ) are becoming more and more recognized as an alternative to reduce dependence on fossil fuels. Currently, two widely recognized  $ESD_s$  are supercapacitors ( $SC_s$ ) and batteries [4,5].  $SC_s$  are an innovative type of  $ESD_s$  that can be recharged using effective capacitor charge/discharge and offer various advantages compared to batteries, such as rapid charging and

discharging abilities, extended cyclic life and higher specific power ( $S_P$ ) [6–8]. Consequently,  $SC_s$  are extensively utilized in various sectors as a means of generating alternative energy and powering intelligent electronic devices.  $SC_s$  can be categorized as electrochemical double-layer capacitors ( $EDLC_s$ ) and pseudocapacitors ( $PC_s$ ).  $EDLC_s$  preserve energy by adsorb-desorb ions at the electrode surface, whereas  $PC_s$  preserve energy through a quick and reverse redox reaction at the electrode surface [9,10]. However, the performance of  $EDLC_s$  is specifically limited by their lower specific capacitance ( $C_s$ ). Pseudocapacitive materials have gained significant attention due to their ability to store charge through a rapid faradaic process, resulting in increased energy density compared to carbon-based materials. The electrode and electrolyte have a remarkable effect on the electrical features of  $SC_s$  [11,12].

Ruthenium oxide ( $RuO_2$ ) is a significant metal oxide utilized in

\* Corresponding author.

E-mail address: [abdulkhalilq78965@gmail.com](mailto:abdulkhalilq78965@gmail.com) (A. Khalil).

pseudocapacitors electrodes due to its distinctive characteristics; although, because of its higher cost, its commercial usage is not easy. Transition metal chalcogenides (TMC<sub>s</sub>) have taken the attraction of researchers to pseudocapacitive electrodes such as oxides, sulfides and tellurides etc, because of their several active sites, smaller ion diffusion ways and electric conductivity [13,14]. For ESD<sub>s</sub> transition metal selenides (TMS<sub>s</sub>) have been proposed as favourable electrode materials. This is because TMS<sub>s</sub> have a synergistic surface with various metallic ions, which can significantly enhance their electrochemical properties, including the redox-active zone, S<sub>p</sub>, cyclic stability and specific energy (S<sub>E</sub>) [15,16]. Tin is an n-type semiconductor that has excellent electrochemical capacitive properties. Tin oxide's distinctive electrical and conductive characteristics have attracted significant interest due to its versatility in various applications, such as electrode materials, electronic devices and solar cells [17,18]. Compared to other electrode materials, transition metal chalcogenides (TMC<sub>s</sub>) exhibited the pseudocapacitive characteristics with high redox reaction, which enhance the conductivity, specific energy (S<sub>E</sub>) with high specific capacitance (C<sub>s</sub>). However, metal selenides and tellurides are highly significant chalcogenide compounds with exceptional electrochemical characteristics [19,20]. Further, Tin selenide (SnSe) combined with manganese telluride (MnTe) have been suggested as excellent electrode materials for energy storing devices (ESD<sub>s</sub>) due to their synergistic effect with several metallic ions and high oxidation reduction process, which significantly increase the electrochemical characteristics, like the redox-active zone, conductivity and cyclic stability [21,22]. Consequently, several techniques are utilized to increase the efficiency of electrode materials, including modification of their structure, fabrication of composites and elemental by doping [23–25]. Considerable advancements have been achieved in the development of composites consisting of two pseudocapacitive materials. Scientists are working on developing electrode materials, specifically composites with other TMC<sub>s</sub>, to enhance the S<sub>E</sub> of SC<sub>s</sub> [26,27]. Various electrode materials utilizing TMC<sub>s</sub> have been reported up until now for SC<sub>s</sub>, such as Abdullah et al. prepared Ag<sub>2</sub>Se/SnTe for SC<sub>s</sub> that demonstrated C<sub>s</sub> 1560.31 F/g, S<sub>E</sub> 99.75 Wh/kg, S<sub>p</sub> of 1356.80 W/kg at 4.0 A/g and C<sub>s</sub> retained of 95.0 % after 5000th cycle in 2 M KOH [28]. Zhao et al. fabricated NiSe/ZnSe that exhibited C<sub>s</sub> of 651.50 mAh/g at 1.0 A/g and C<sub>s</sub> retained 97.6 % after the 2000th cycle [29]. Liu et al. fabricated NiSe/NiTe<sub>2</sub> electrode material for SC<sub>s</sub> that exhibit C<sub>s</sub> 1782.61 F/g at 1.0 A/g, S<sub>E</sub> 23.25 Wh/kg and C<sub>s</sub> retained 84.8 % over 20,000<sup>th</sup> cycles [30]. Ahmed et al. prepared SnSe/rGO that demonstrated C<sub>s</sub> of 568 F/g at 1.0 A/g and S<sub>E</sub> 30.50 Wh/kg at a S<sub>p</sub> of 1.0070 kW/kg [31]. Ashwini et al. fabricated Te/rGO electrode material that showed C<sub>s</sub> 460 F/g at 5.0 mV/s [32]. This research lies in the production of electrode materials that effectively reduce the aggregation of SnSe and MnTe. The MnTe-modified SnSe nanocomposite has a larger surface area, which enables greater absorption of electrolyte ions. Both MnTe and SnSe electrode materials offer distinct advantages that make them suitable for the cost-effective commercial production of SC<sub>s</sub>.

In the present work, the SnSe–MnTe (SSMT) nanocomposite material was successfully synthesized using the sonication synthesis procedure. The structural and morphological characteristics of the manufactured SnSe, MnTe and SSMT nanocomposite have been analysed utilizing a variety of analytical methods. SSMT nanocomposite demonstrated excellent electrochemical performance and displayed specific capacitance (C<sub>s</sub>) 1502 F/g at 1.0 A/g and retained longer stability after the 5000th cycle. Thus, this study illustrates the significance of metal chalcogenides while presenting an innovative approach for energy storing applications using an affordable preparation route.

## 2. Experimental

### 2.1. Reagents

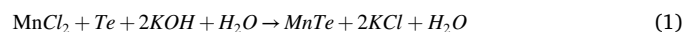
Ethanol (C<sub>2</sub>H<sub>5</sub>OH, Sigma Aldrich, >98.0 %), tellurium powder (Te, AlanaR, >99.0 %), potassium hydroxide (KOH), Merck, >85.0 %),

hydrochloric acid (HCl, Merck, >37.0 %), hydrazine monohydrate (N<sub>2</sub>H<sub>4</sub>·H<sub>2</sub>O, Sigma Aldrich, >64 %), tin chloride (SnCl<sub>2</sub>, Sigma Aldrich, >99 %), manganese chloride (MnCl<sub>2</sub>, Merck, >99.0 %), selenium powder (Se, AlanaR, >99.0 %) and deionized water (DI H<sub>2</sub>O) were employed in the manufacturing process of SnSe–MnTe without performing any extra purification processes.

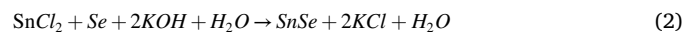
### 2.2. Synthesis of MnTe and SnSe

A homogenous solution was formed by utilizing DI H<sub>2</sub>O 50 mL with tellurium powder and MnCl<sub>2</sub> (0.1 M) and stirring consistently for 30 min to fabricate MnTe. Next, 6.0 M KOH solution was added dropwise while mixing continuously. After that, hydrazine 2 mL was included as a strong reducing agent to the reaction mixture while vigorously stirring continued. Finally, the acquired material was transferred in the autoclave and preserved in the oven for 7 h at 433.15 K. The resultant material was washed properly multiple times with DI H<sub>2</sub>O and C<sub>2</sub>H<sub>5</sub>OH before drying for 12 h at 343.15 K. The material that had been dehydrated was grinded and kept in plastic vials to protect it from the moisture in the air. However, pure SnSe was similarly made using the previously described technique and the same parameters, utilizing tin chloride (SnCl<sub>2</sub>) and selenium powder and the chemical reactions that occurred during the production process are presented below as expressions 1 and 2 [33].

#### 2.2.1. For MnTe



#### 2.2.2. For SnSe



### 2.3. Preparation of SnSe–MnTe

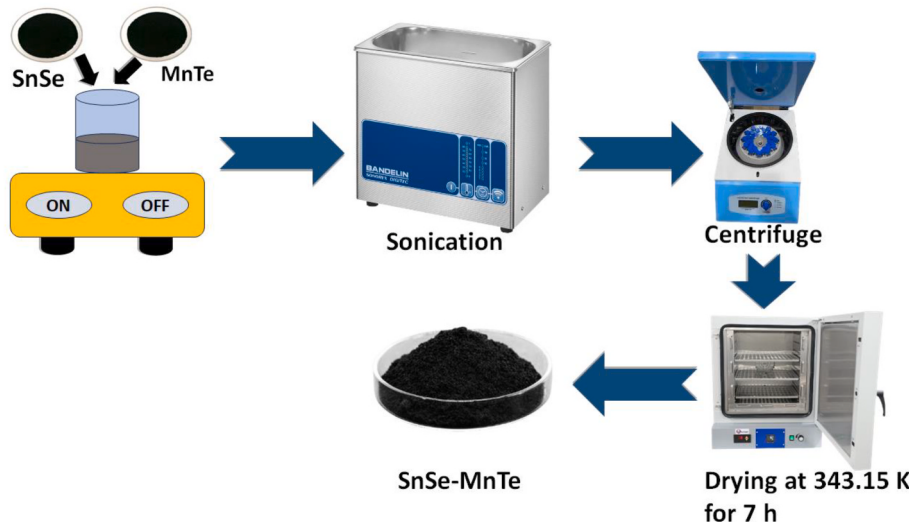
The standard method for creating the SnSe–MnTe (SSMT) nanocomposite involved mixing MnTe (0.3 g) and SnSe (0.3 g) with 50 mL DI (H<sub>2</sub>O), while stirring constantly. The final solution was put into a sonicator (PC5 model, BANDELIN, Germany) and sonicated for 30 min and at the end centrifugation was used to separate the final products, which were then rinsed with C<sub>2</sub>H<sub>5</sub>OH and DI H<sub>2</sub>O and solution suspension dehydrated in oven at 343.15 K for 7 h. The graphical representation of SSMT nanocomposite synthesis is represented in Scheme 1.

### 2.4. Material characterizations

The material crystalline structure was investigated with X-ray diffraction (XRD) utilizing a Bruker D-2 X-ray diffractometer (D/Max 2500 PC, Germany, Rigaku Corporation) that was tested with CuK $\alpha$  radiations with a wavelength (0.15406 nm). All of the manufactured electrode material's interface morphology was evaluated using scanning electron microscopy (SEM, Quanta 200, Czech). Raman investigations were executed with (LabRAM HR, 532 nm, Spain) laser stimulation implemented to study the material quality, particularly carbon disorders and imperfections in samples. The purity of the sample verified by Energy-dispersive X-ray diffraction (EDX) (Quanta FEG-200). The Brunauer Emmett Teller (BET, Nova2200e Quantachrome) was employed to measure electrode material textural characteristics.

### 2.5. Electrochemical measurements

Employing a Metrohm auto lab (PG STAT-204) that has 3-electrode systems: a reference electrode silver/silver chloride (Ag/AgCl), a working electrode and a platinum (Pt) wire that will serve as a counter electrode. A small area of 1 × 1 cm<sup>2</sup> of nickel foam (NF) was utilized to fabricate a functioning electrode. NF was the conductive substrate



**Scheme 1.** Graphical presentation of SnSe–MnTe nanocomposite via sonication method.

utilized in the experiment's first stage, to activate the NF, it was cleaned via ethanol and deionized water solution. After that, NF was dried for 30 min at 313.15 K in an oven. A 5  $\mu\text{L}$  water solution containing 5 mg of electrode material was used to create the homogenous paste, additionally, the electrode was created on NF using the drop-casting process and dried in the oven at 343.15 K for 12 h then used for electrochemical analysis. To evaluate the electrochemical efficiency in KOH (2.0 M) basic media, cyclic voltammetry (CV), chronoamperometry, electrochemical impedance spectroscopy (EIS) and galvanostatic charging-discharging (GCD) were utilized.

Employing a typical 3-electrode setup in KOH (2.0 M), the electrode was examined electrochemically using an electrochemical workstation (PG STAT-204, Netherlands). Galvanostatic charging/discharging (GCD), electrochemical impedance spectroscopy (EIS) and cyclic voltammetry (CV) investigations were utilized to evaluate the synthesized materials' electrochemical capabilities. In the CV analysis potential window and various sweep rate were utilized to investigate the capacitive properties of the synthesized materials. In 0–0.65 V vs Ag/AgCl potential window materials shows better faradaic behaviour in this region. However, the smallest scan rate (10 mV/s) was employed due to electrolyte ions have sufficient time for penetrations on the electrode interface responsible for greater specific capacitance. Moreover, as the scan rate was increases, the specific capacitance ( $C_s$ ) decreased because of high resistance and high transportation pathways of ion to electrode surface [34,35]. Additionally, the electrode material's specific capacitance ( $C_s$ ) was determined using the following eqn. (3) using the CV analysis [36].

$$C_s = \frac{\int_{V_c}^{V_a} I \times dV}{m \times S \times \Delta V} \quad (3)$$

Here I represent current (A), S (sweep rate), m demonstrates loaded mass, dV and  $\Delta V$  (change in potential window of CV curve).

$$C_s = \frac{\int_{V_c}^{V_a} I \times dV}{S(V_a - V_c)} \quad (4)$$

Where S is the area ( $\text{cm}^2$ ), v is sweeping rate ( $\text{V/s}$ ),  $V_a$  is the anodic potential (V),  $V_c$  is the cathodic potential (V), I (V) is current density ( $j_d$ ) (A) and V is the potential (V).

Additional investigation was conducted on galvanostatic charge/discharge to estimate the specific capacitance ( $C_s$ ), energy ( $S_E$ ) and power ( $S_p$ ) using eqns. (5)–(7), respectively [37,38].

$$C_s = \frac{I \times \Delta t}{m \times \Delta V} \quad (5)$$

Where I represent current (A), dt (change in time (s), m (mass (g) and  $\Delta V$  (potential change).

$$S_E = \frac{C_s \times \Delta V^2}{7.2} \quad (6)$$

$$S_p = \frac{C_s \times \Delta V}{\Delta t} \quad (7)$$

Here,  $\Delta V$  (potential window change during GCD) and  $\Delta t$  (discharging time).

$$C_{As} = \frac{I \times \Delta t}{S \times \Delta V} \quad (8)$$

Where  $C_{As}$  is a real capacitance ( $\text{F/cm}^2$ ), I (current (A)), t (discharging time (s)), S is the geometrical interfacial area of the electroactive materials in the electrodes ( $\text{cm}^2$ ), dV is the change in potential (V).

### 3. Results and discussions

#### 3.1. Material characterizations

X-ray diffraction was used to study the material's crystallinity as well as the phase purity of the SnSe, MnTe and SnSe–MnTe (SSMT) at 20 (20–80°). The diffraction peaks of SnSe at 24.95°, 26.78°, 29°, 31.15°, 37.25°, 39.87°, 41.45°, 43.54°, 45.98°, 47.90°, 49.04°, 53.84° and 59.64° correspond to the planes (027), (012), (111), (004), (113), (200), (201), (114), (121), (115), (024) and (302) demonstrating the existence of an orthorhombic crystal system, which corresponds to JCPDS: 00-017-0347, represented in Fig. 1(a). For MnTe, the reflection peaks are seen at 31.93°, 33.07°, 42.15°, 47.90°, 50.34°, 56.37°, 59.95° and 61.61° correspond to the plane (111), (210), (121), (002), (301), (131), (022) and (321) planes showed an orthorhombic crystal structure, which was in an excellent match with JCPDS: 00-040-1195. The presence of the diffraction peaks from both phases in the SSMT XRD diffraction pattern demonstrated that the nanocomposite materials had been successfully synthesized [39].

The Raman spectra of SnSe Fig. 1(b) exhibit a peak at 135–156  $\text{cm}^{-1}$ , originated from the  $\text{A}_{g1}$  vibration mode attribute of SnSe [40]. Moreover, the Raman spectra were obtained and analysed in order to investigate the vibrational modes of the MnTe. The  $\text{B}_2$  mode of MnTe can be determined at 189.34  $\text{cm}^{-1}$  peak and Raman peaks at 126.13 and

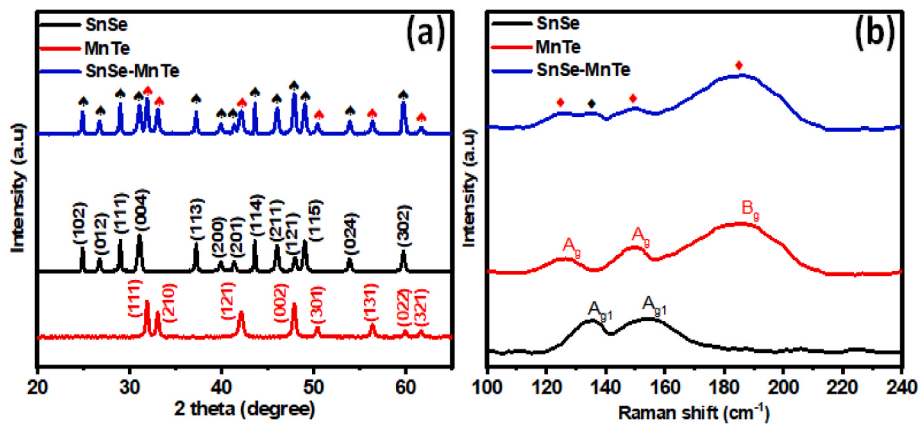


**Fig. 1.** (a) XRD diffractogram of SnSe, MnTe and SnSe–MnTe and (b) RAMAN spectrum of SnSe, MnTe and SnSe–MnTe nanocomposite.

150.2 cm<sup>-1</sup> associated to the A<sub>g</sub> vibration mode as represented in Fig. 1(b) [41,42]. Furthermore, the absence of distinctive peaks associated with crystalline phases like MnO<sub>2</sub> or MnO<sub>3</sub> suggests that MnTe created using the simple hydrothermal process is pure and free from any further contaminants. The Raman shift peak indicates the successful incorporation of SSMT in the nanocomposite material. This result furthermore verifies the development of the SSMT nanohybrid.

The SEM technique was employed to evaluate the interfacial morphology of SnSe, MnTe and SSMT, obtained findings are depicted in Fig. 2(a–c). Fig. 2(a) represents the structure of SnSe, showing agglomerated nanoparticles with uneven shapes. In addition, MnTe exhibited nano-sticks with a significant interfacial area, which is crucial for the electrochemical procedure, as depicted in Fig. 2(b). The SSMT nanocomposite developed, resulting in the decoration of nanoparticles on the nano-sticks. This decoration has a synergistic impact on the electrochemical characteristics of the SnSe and MnTe combination, as depicted in Fig. 2(c). Additionally, the elemental composition of the SSMT nanohybrid in Fig. 2(d) was examined using EDX. The EDX spectra of the SSMT nanocomposite show separate peaks for carbon (C), oxygen (O), manganese (Mn), tin (Sn), tellurium (Te) and selenium (Se) [43,44]. Furthermore, the no additional peaks in the spectra of the manufactured SSMT nanocomposite material verify the purity.

(O), manganese (Mn), tin (Sn), tellurium (Te) and selenium (Se) [43,44]. Furthermore, the no additional peaks in the spectra of the manufactured SSMT nanocomposite material verify the purity.

The interfacial characteristics of the manufactured items were assessed utilizing the BET approach, which involves analysing the absorption and desorption of N<sub>2</sub>. The existence of charged species enhances the active sites and interface area. The BET isotherms exhibited a type III loop, which is characteristic of a mesoporous interface, as depicted in Fig. 2(e). Mesoporous substance possesses a significant quantity of nanoscale electrochemical sites and a significant interfacial area. The interfacial area of the SSMT nanocomposite (61.43 m<sup>2</sup>/g) was greater than those of SnSe (23.89 m<sup>2</sup>/g) and MnTe (39.58 m<sup>2</sup>/g) and the enhanced interfacial area was because of the combining effect of SnSe and MnTe. SSMT nanocomposite shows an enhanced active site associated with SnSe, MnTe, that is beneficial for the absorption of different active species and would enhance the electrochemical characteristics.

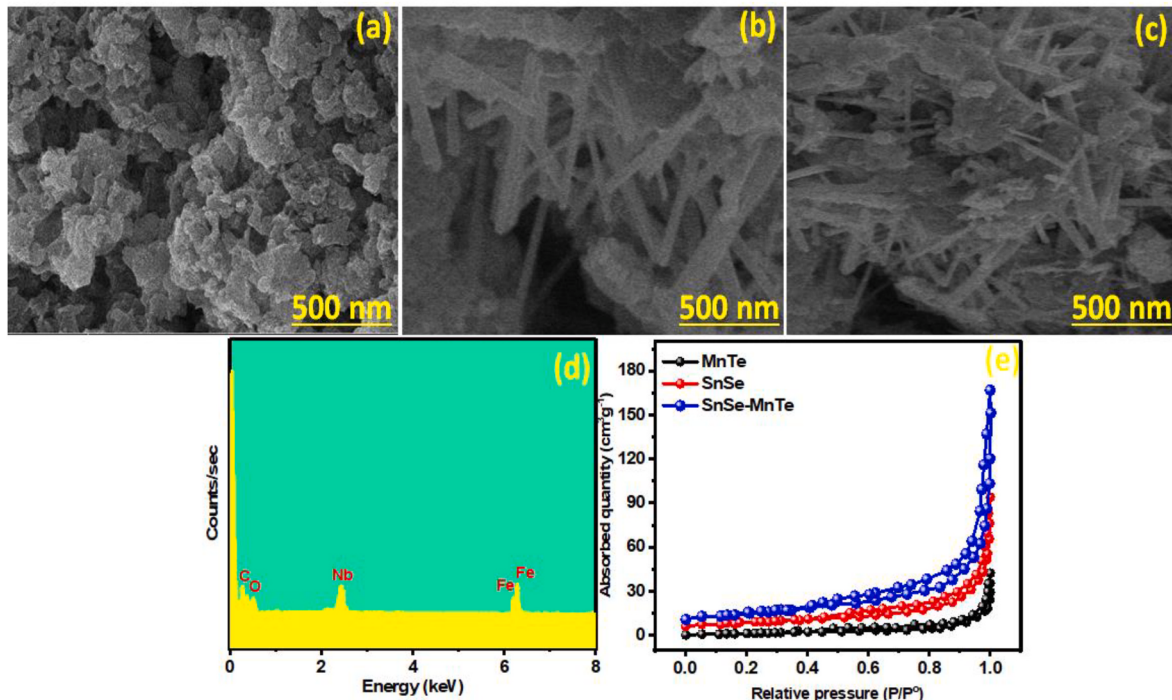


**Fig. 2.** SEM of (a) SnSe, (b) MnTe, (c) SnSe–MnTe, (d) EDX of SnSe–MnTe nanocomposite, (e) BET of SnSe MnTe and SnSe–MnTe nanocomposite.

#### 4. Electrochemical characterizations

To investigate  $C_s$  of SnSe, MnTe and SnSe–MnTe (SSMT) nanocomposite, CV investigations were performed employing 3-electrode systems in solution (2 M KOH). The CV polarisation curves of SnSe, MnTe and SSMT at sweeping rates (10–40 mV/s) at 0–0.65 V are represented in Fig. 3(a–c). All of the manufactured electrode's redox peaks show the reversible redox processes including the faradaic capacitive behaviour of the electrodes. The specific capacitance ( $C_s$ ) of SnSe, MnTe and SSMT electrode materials are 430.93, 905.65 and 1499.56 F/g at 10.0 mV/s, correspondingly. SSMT demonstrated the high  $C_s$  because of its increased electrochemical sites and synergistic impact of bimetals, which create additional space for the electrolyte ions intercalation and a bigger interfacial area [45]. Khot et al. recently fabricated Dy<sub>2</sub>Se<sub>3</sub>/rGO for SC<sub>s</sub> that demonstrated  $C_s$  289.0 F/g at 5.0 mV/s sweep rate and  $C_s$  retained 89.0 % after 5000th cycle and showed pseudo-capacitive [46]. Salam et al. fabricated NiCo<sub>2</sub>S<sub>4</sub>/rGO via hydrothermal method that showed  $C_s$  of 588 F/g at 1.0 A/g and demonstrated the pseudo-capacitive behaviour [47]. Areal capacitance of SnSe, MnTe and SnSe–MnTe nanocomposite 0.260, 0.547 and 0.907 F/cm<sup>2</sup>, respectively calculated from eqn. (4). Cathodic peak shifted -ve potential area and anodic peaks shifted to + ve potential, with faster sweep rates. The slow faradaic process at lower scan rates may be because of the  $C_s$  of all the manufactured electrode materials, which lower as the scan rate rises, as seen in Fig. 3(d). Additionally, as illustrated in Fig. 3(e), the ratio anodic peak (I<sub>pa</sub>) and cathodic peak current (I<sub>pc</sub>) demonstrated a linear relationship with the sweep rate. Anodic peak current enhanced and lower peak current reduced as the scan rate increased as demonstrated by the linear plots of I<sub>pa</sub> and I<sub>pc</sub>. The investigations of CV studies demonstrated that for all materials, the oxidation/reduction peaks moved toward high potentials and low potential regions, respectively, as the sweep rate enhanced and the synthesized SSMT nanocomposite  $C_s$  decreased as the scan rate increased [48].

The charging/discharging behaviour of SnSe, MnTe and SSMT nanocomposite was obtained by GCD investigation (1–3.0 A/g), as illustrated in Fig. 4(a–c), correspondingly. The observation that SSMT exhibits the highest discharge rate compared to SnSe and MnTe indicates that the existence of a discharging voltage curve at j<sub>d</sub> indicates a redox reaction within the abilities of the CV. Furthermore, as represented in Fig. 4(d), the electrocatalyst's  $C_s$  decreased as the j<sub>d</sub> increased.

Using eqn. (5), the  $C_s$  of the SnSe, MnTe and SSMT were calculated 609.56, 931.72 and 1502 F/g, respectively. The synergistic behaviour of the tin and manganese elements with Se and Te, which supply additional electrons and improve the interfacial area, results in increased  $C_s$  of SSMT nano-sticks. This increases the  $C_s$  of SSMT nanocomposite which is higher than SnSe and MnTe due to electron penetration. The specific energy (S<sub>E</sub>) and specific power (S<sub>P</sub>) are identified from the GCD curve utilizing eqns. (6) and (7), respectively. The excellent morphology and enhanced surface area of SSMT resulted in S<sub>E</sub> of 61.05 Wh/kg and S<sub>P</sub> of 270.5 W/kg at 1.0 A/g. Dorsa et al. fabricated NiTe<sub>2</sub>/MnTe for SC<sub>s</sub> that showed  $C_s$  of 1325.51 C/g at 1.0 A/g, S<sub>E</sub> 62.31 Wh/kg, S<sub>P</sub> 890.0 W/kg and  $C_s$  retained 85.75 % after 7000th cycle with a small  $C_s$  decrease of 8.14 % at 7.50 A/g [49]. Wan et al. prepared CoFe<sub>2</sub>Se<sub>4</sub>/CoNi–CH that exhibited  $C_s$  of 218.6 mAh/g at 1.0 A/g, S<sub>E</sub> of 67.30 Wh/kg and S<sub>P</sub> 765.90 W/kg [50]. The areal capacitance of SnSe, MnTe and SnSe–MnTe nanocomposite are 0.927, 2.03 and 4.390 F/cm<sup>2</sup> at 1 A/g is investigated through eqn. (8). Table 1 present the comparison of the manufactured electrodes. The Ragone graphs in Fig. 4(e) explain the correlation between the S<sub>E</sub> and S<sub>P</sub>. Following these investigations, it suggested that SSMT nanocomposite is a viable candidate for SC<sub>s</sub> applications [51].

The resistance and capacitance characteristics of electrode materials were analysed utilizing the EIS investigation. Nyquist plot of the produced electrodes of SnSe, MnTe and SnSe–MnTe (SSMT) nanocomposite at a frequency (100 Hz–100 kHz) as displayed in Fig. 5(a). SnSe, MnTe and SSMT nanocomposite measured resistances show a distinct and well-defined semicircle pattern. Impedance curve slope present Warburg resistance (Z<sub>ω</sub>) in the lower-frequency range caused by OH<sup>-</sup> ions diffusion resistance and electrolyte. Charge transfer resistance (R<sub>ct</sub>) associated to the size of the semicircle size and solution resistance (R<sub>s</sub>) associated with real axis intercept (Z') [63]. SnSe, MnTe and SSMT nanocomposite exhibiting R<sub>ct</sub> of 1.25, 0.69 and 0.30 Ω, respectively and the EIS profile slope line towards 90° of the SSMT nanocomposite, signifying the KOH ions fast diffusion on the interface of the electrode materials. Furthermore, the results demonstrate the presence of nano-sticks, which increased the electrolyte's interfacial area, is the reason why the R<sub>ct</sub> of the SSMT nanocomposite is lower than pristine SnSe and MnTe. This suggests that the capacitive properties of the SSMT nanocomposite electrode have been improved, while its inherent resistance has been decreased [64]. Moreover, the EIS parameters were utilized to investigate the electrochemical behaviour of the SnSe–MnTe

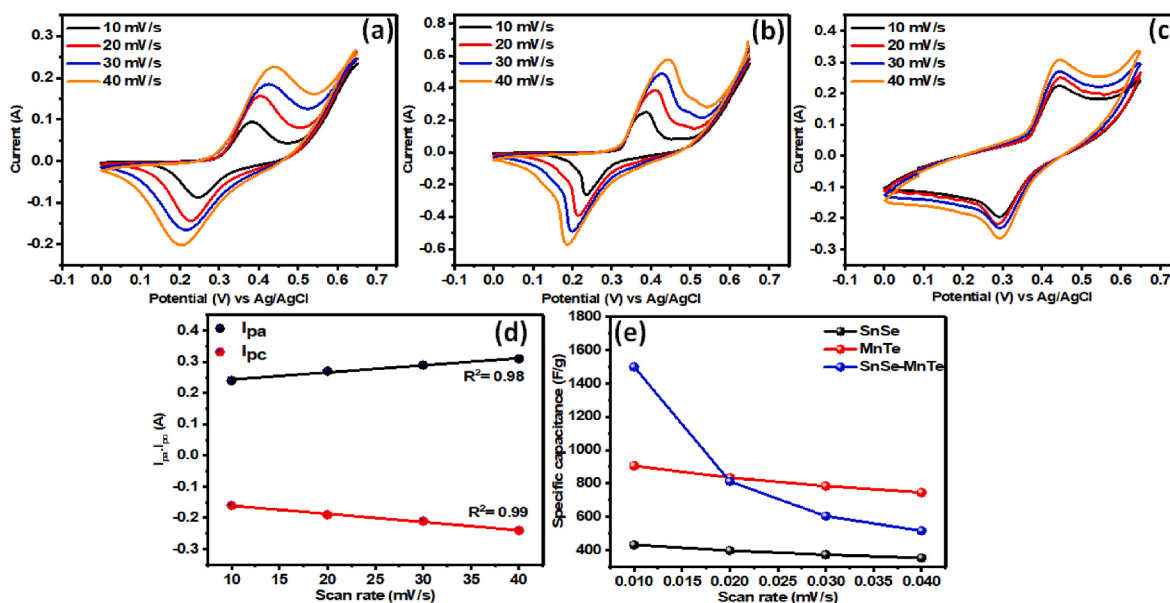


**Fig. 3.** CV of (a) SnSe, (b) MnTe, (c) SnSe–MnTe nanocomposite, (d) anodic peak current (I<sub>pa</sub>) and cathodic peak current (I<sub>pc</sub>) vs sweep rate of SnSe–MnTe nanocomposite and (e) specific capacitance vs scan rate of all fabricated materials.

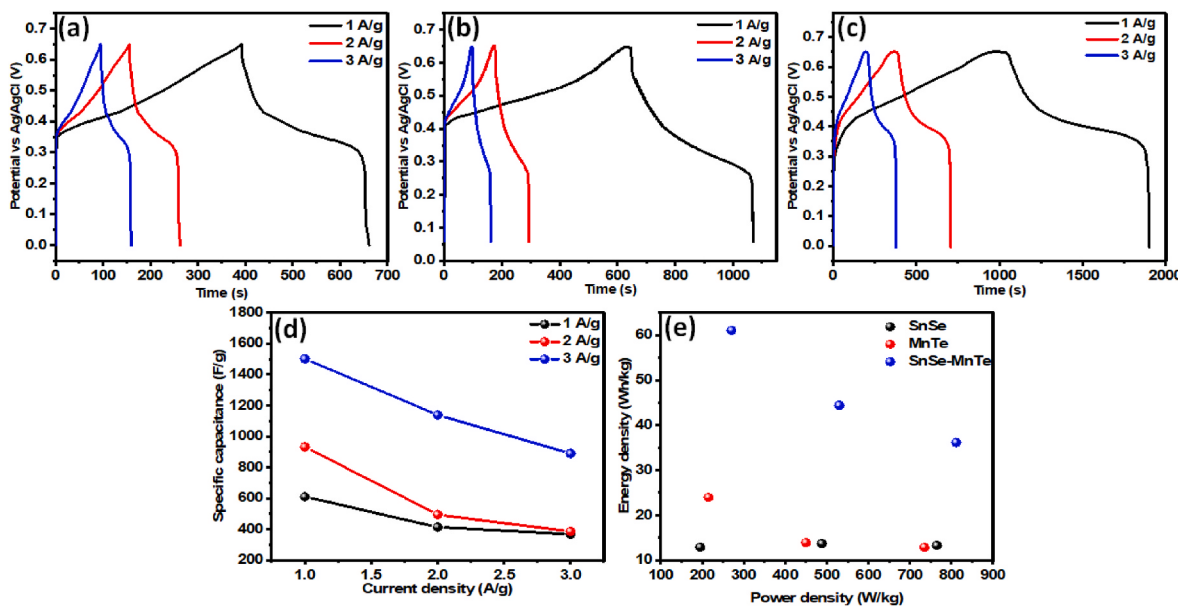


**Fig. 4.** GCD of (a) SnSe, (b) MnTe, (c) SnSe–MnTe nanocomposite, (d) specific capacitance vs current density (e) Ragone plot of SnSe, MnTe and SnSe–MnTe nanocomposite.

**Table 1**  
Comparative analysis of manufactured SnSe–MnTe nanocomposite electrode with other previous electrodes for SC<sub>s</sub> application.

Sr. No.	Materials	Specific capacitance (F/g)	Current density (A/g)	Reference
1	MoS <sub>2</sub> /Te	402.53	1	[52]
2	CoTe <sub>2</sub> /CoSe <sub>2</sub>	951	5 mV/s	[53]
3	SnTe/SnSe	1276	1	[54]
4	Se/Te	1456	1	[55]
5	ZnSe/MnSe	1439.98	1	[56]
6	MnSe/WSe <sub>2</sub>	1326	1	[40]
7	NiSe <sub>2</sub> /CdSe	90	20	[57]
8	SnSe	617.9	2 mV/s	[58]
9	Ag <sub>2</sub> Te	711.86	1	[59]
10	ZnSe/FeSe	1419.8	1	[60]
11	SnSe	214.3	1	[61]
12	NiSe	6.81	5 mA/cm <sup>2</sup>	[62]
13	SnSe–MnTe	1502	1	Present work

electrode before and after the stability investigation. Fig. 5(b) represents the associated Nyquist plot developed in the frequency (100 Hz–100 kHz) at an applied potential. SnSe–MnTe nanocomposite shows  $R_{ct}$  was 0.27 Ω before and 0.41 Ω after stability attributed to blockage of the active sites with electrolyte ions. Nyquist plot comprises a semi-arch in the higher-frequency zone and a straight line is acquired in the lower-frequency zone. From Fig. 5(c), it is evidence that the phase angle at the tail is nearly 55° and more toward the 90° suggest the pseudo-capacitive behavior of SnSe–MnTe electrodes [65,66]. Chronoamperometry was used to investigate the electrochemical stability of SSMT at a constant potential (0.75 V). As depicted in Fig. 5(d), the chronological  $j_d$  of SSMT declines only at 5 h and then stabilizes for up to 40 h. SSMT nanocomposite, on the other hand, exhibits stable behaviour over 40 h with a slight decrease in  $j_d$  of 40 mA/cm.

The stability cycles based on the nanocomposite materials CV investigation over the 5000th cycle is represented in Fig. 6(a) CV stability of the SSMT with a small change in the  $j_d$  after the 5000th cycle. After the CV stability test, there was a very slight change in current seen in the voltammograms of the manufactured materials. A negligible change in the nanocomposite materials' performance was due to charge

deposition at the surface of the electrocatalytic species and blocking the active sites. Additionally, the materials' structural stability was examined using XRD analysis as shown in Fig. 6(b), diffractograms showed that the structures stayed similar, with a minor transform in intensity caused by the electrochemical active sites being covered in charge accumulation and after stability, the SSMT nanocomposite XRD diffractogram illustrates that the electrode materials have a robust structure. As represented in Fig. 6(c and d), SSMT nanocomposite morphology stability was further investigated using SEM after structural stability. After the long-term stability investigation small changes occurred in the morphology of the materials was identified because of the existence of several adsorbed species like OH<sup>-</sup> ions on the electrode interface, which block the electrode material active sites.

## 5. Conclusion

Utilizing the sonication method, SnSe, MnTe and SnSe–MnTe (SSMT) nano-sticks for energy storage devices have been successfully synthesized. The SSMT electrode's analytical result showed a nano-sticks shape with an interfacial area of 23, 39 and 61 m<sup>2</sup>/g. The SSMT gained specific capacitance 1502 F/g at 1.0 A/g, specifically greater than MnTe, according to electrochemical studies. Therefore, SSMT electrode shows benefits such as more active sites, enhanced interfacial area and efficient electron transportation. This concept should make it possible to develop new nanostructured materials that have a lot of capacity in energy-storing devices such as supercapacitors.

## Compliance with ethical standards

The ethical rules of the journal are adhered to by this paper.

## CRediT authorship contribution statement

**Abdul Khalil:** Writing – original draft. **Meznah M. Alanazi:** Conceptualization. **Shaimaa A.M. Abdelmohsen:** Formal analysis. **Saeed D. Alahmari:** Funding acquisition. **Khalid I. Hussein:** Investigation. **A.M.A. Henaish:** Funding acquisition. **Muhammad Abdulla:** Supervision.

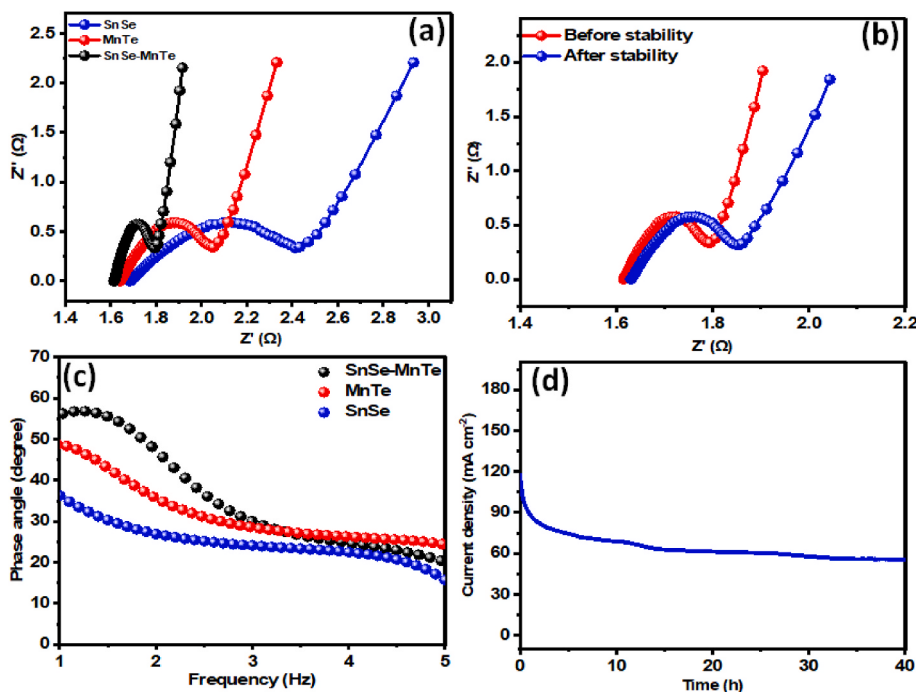


**Fig. 5.** (a) EIS of SnSe, MnTe and SnSe–MnTe nanocomposite, (b) EIS before and after stability of SnSe–MnTe nanocomposite (c) Bode plot of SnSe, MnTe and SnSe–MnTe nanocomposite (d) Chronoamperometry of SnSe–MnTe nanocomposite.

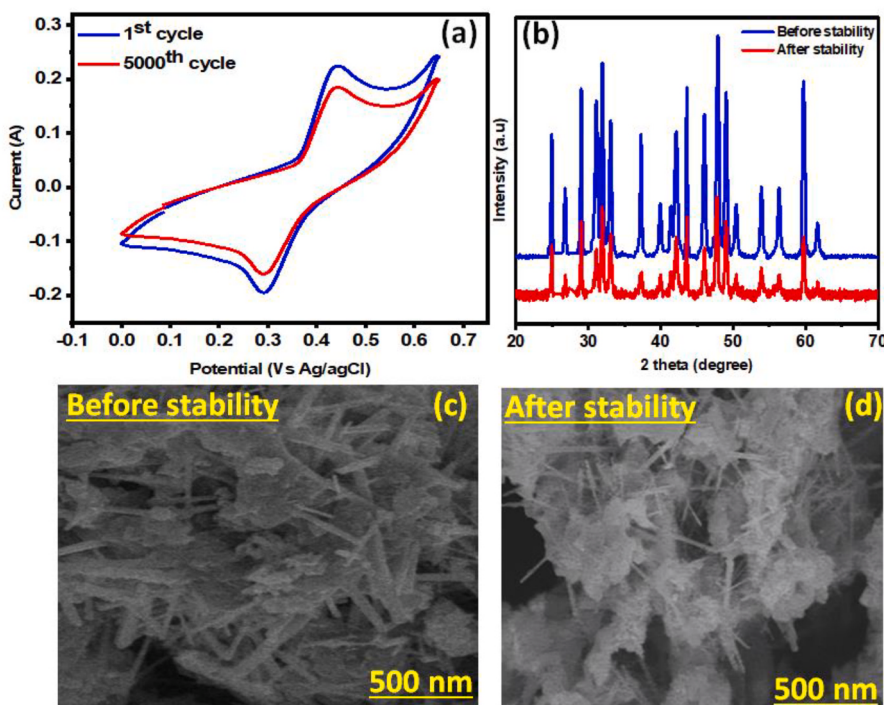


**Fig. 6.** (a) CV stability of SnSe–MnTe nanocomposite, (b) XRD stability of SnSe–MnTe nanocomposite, (c) SEM images of SnSe–MnTe nanocomposite before stability, (d) SEM images of SnSe–MnTe nanocomposite after stability.

#### Declaration of competing interest

The authors declare that they have no known competing financial interests or personal relationships that could have appeared to influence the work reported in this paper.

#### Data availability

Data will be made available on request.

#### Acknowledgments

The authors extend their appreciation to the Deanship of Scientific

Research at King Khalid University for funding this work through large group Research Project under grant number RGP.2/589/44. The authors express their gratitude to Princess Nourah bint Abdulrahman University Researchers Supporting Project number (PNURSP2024R132), Princess Nourah bint Abdulrahman University, Riyadh, Saudi Arabia.

## References

- [1] W. Kuang, H. Wang, X. Li, J. Zhang, Q. Zhou, Y. Zhao, Application of the thermodynamic extremal principle to diffusion-controlled phase transformations in Fe-C-X alloys: modeling and applications, *Acta Mater.* 159 (2018) 16–30, <https://doi.org/10.1016/J.ACTAMAT.2018.08.008>.
- [2] D. Yu, X. Zhong, D. Liu, Y. Liang, The effects of Bi<sub>2</sub>O<sub>3</sub> on the selective catalytic reduction of NO by propylene over Co<sub>3</sub>O<sub>4</sub> nanoplates, *RSC Adv.* 9 (2019) 32232–32239, <https://doi.org/10.1039/C9RA03956B>.
- [3] B. bin Sui, L. Sha, P. fei Wang, Z. Gong, Y. hang Zhang, Y. han Wu, L. na Zhao, J. jie Tang, F. nian Shi, In situ zinc citrate on the surface of Zn anode improves the performance of aqueous zinc-ion batteries, *J. Energy Storage* 82 (2024) 110550, <https://doi.org/10.1016/J.JEST.2024.110550>.
- [4] J. Kumar, H.J. Jung, R.R. Neiber, R.A. Soomro, Y.J. Kwon, N.U. Hassan, M. Shon, J. H. Lee, K.Y. Baek, K.Y. Cho, Recent advances in oxygen deficient metal oxides: opportunities as supercapacitor electrodes, *Int. J. Energy Res.* 46 (2022) 7055–7081, <https://doi.org/10.1002/ER.7675>.
- [5] A. Sandoval-González, E. Bustos, C. Martínez-Sánchez, Basic and advanced considerations of energy storage devices, *eng. Mater* (2022) 63–80, [https://doi.org/10.1007/978-3-030-98021-4\\_4/COVER](https://doi.org/10.1007/978-3-030-98021-4_4/COVER).
- [6] Y. Zhang, X. He, X. Cong, Q. Wang, H. Yi, S. Li, C. Zhang, T. Zhang, X. Wang, Q. Chi, Enhanced energy storage performance of polyethersulfone-based dielectric composite via regulating heat treatment and filling phase, *J. Alloys Compd.* 960 (2023) 170539, <https://doi.org/10.1016/J.JALLCOM.2023.170539>.
- [7] M. Hussain, S.D. Alahmari, F.F. Alharbi, S.R. Ejaz, M. Abdullah, S. Aman, A.G. Al-Sehemi, A.M.A. Henaish, A. Sadaf, H.M.T. Farid, Hydrothermal synthesis of the Ni<sub>5</sub>/g-C<sub>3</sub>N<sub>4</sub> nanohybrid electrode material for supercapacitor applications, *J. Energy Storage* 80 (2024) 110289, <https://doi.org/10.1016/J.JEST.2023.110289>.
- [8] L. Zhu, Z. Li, K. Hou, Effect of radical scavenger on electrical tree in cross-linked polyethylene with large harmonic superimposed DC voltage, *High Volt.* 8 (2023) 739–748, <https://doi.org/10.1049/HVE2.12302>.
- [9] S.M. Ali, H. Kassim, Z.A.M. Alaizeri, M. Shahabuddin, Enhanced electrochemical performance of novel nanoarchitectonics tin selenide (SnSe/rGO) pseudocapacitive material for energy storage application, *J. Energy Storage* 73 (2023) 109163, <https://doi.org/10.1016/J.JEST.2023.109163>.
- [10] J. Yuan, Y. Li, M. Wang, X. Huang, T. Zhang, K.H. Xue, J. Yuan, J. Ou-Yang, X. Yang, X. Xiao, B. Zhu, Ultrasound: a new strategy for artificial synapses modulation, *InfoMat* (2024) e12528, <https://doi.org/10.1002/INF2.12528>.
- [11] Y. Hua, F. Li, N. Hu, S.Y. Fu, Frictional characteristics of graphene oxide-modified continuous glass fiber reinforced epoxy composite, *Compos. Sci. Technol.* 223 (2022) 109446, <https://doi.org/10.1016/J.COMPSCITECH.2022.109446>.
- [12] S. Yang, Z. Huang, Q. Hu, Y. Zhang, F. Wang, H. Wang, Y. Shu, Proportional Optimization Model of Multiscale Spherical BN for Enhancing Thermal Conductivity, *ACS Applied Electronic Materials* 4 (9) (2022) 4659–4667, <https://doi.org/10.1021/acsealm.2c00878>.
- [13] D. Liu, L. Xu, J. Xie, J. Yang, A perspective of chalcogenide semiconductor-noble metal nanocomposites through structural transformations, *Nano Mater. Sci.* 1 (2019) 184–197, <https://doi.org/10.1016/J.NANOMS.2019.03.005>.
- [14] C. Zhu, Y. Hao, H. Wu, M. Chen, B. Quan, S. Liu, J. Qu, Self-Assembly of Binderless MXene Aerogel for Multiple-Scenarios and Responsive Phase Change Composites with Ultrahigh Thermal Energy Storage Density and Exceptional Electromagnetic Interference Shielding, *Nano-Micro Letters* 16 (1) (2024) 57, <https://doi.org/10.1007/s40820-023-01288-y>.
- [15] T. Zahra, M.M. Alanazi, A. Gassoumi, S.A.M. Abdelmohsen, M. Abdullah, S. Aman, A.M.A. Henaish, H.M.T. Farid, High-performance MoO<sub>3</sub>/g-CN supercapacitor electrode material utilizing MoO<sub>3</sub> nanoparticles grafted on g-CN nanosheets, *Diam. Relat. Mater.* 143 (2024) 110892, <https://doi.org/10.1016/J.DIAMOND.2024.110892>.
- [16] X. Zheng, C. Han, C. Lee, W. Yao, C. Zhi, Y. Tang, Materials challenges for aluminum ion based aqueous energy storage devices: Progress and prospects, *Progress in Materials Science* 143 (2024) 101253. <https://doi.org/10.1016/j.pmatsci.2024.101253>.
- [17] T.K. Shivasarma, L.K. Bommineedi, B.R. Sankapal, Pseudocapacitive nanostructured silver selenide thin film through room temperature chemical route: first approach towards supercapacitive application, *Inorg. Chem. Commun.* 135 (2022) 109083, <https://doi.org/10.1016/J.INOCHE.2021.109083>.
- [18] M. Hussain, B.M. Alotaibi, A.W. Alrowaily, H.A. Alyousef, M.F. Alotiby, M. Abdullah, A.G. Al-Sehemi, A.M.A. Henaish, Z. Ahmad, S. Aman, Synthesis of high-performance supercapacitor electrode materials by hydrothermal route based on ZnSe/MnSe composite, *J. Phys. Chem. Solid.* 188 (2024) 111919, <https://doi.org/10.1016/J.JPCS.2024.111919>.
- [19] P. Zhou, L. Fan, J. Wu, C. Gong, J. Zhang, Y. Tu, Facile hydrothermal synthesis of NiTe and its application as positive electrode material for asymmetric supercapacitor, *J. Alloys Compd.* 685 (2016) 384–390, <https://doi.org/10.1016/J.JALLCOM.2016.05.287>.
- [20] H. Wang, Z. Huang, X. Zeng, J. Li, Y. Zhang, Q. Hu, Enhanced Anticarbonization and Electrical Performance of Epoxy Resin via Densified Spherical Boron Nitride Networks, *ACS Applied Electronic Materials* 5 (7) (2023) 3726–3732, <https://doi.org/10.1021/acsealm.3c00451>.
- [21] R. Yang, W. Yao, L. Zhou, F. Zhang, Y. Zheng, C.S. Lee, Y. Tang, Secondary amines functionalized organocatalytic iodine redox for high-performance aqueous dual-ion batteries, *Adv. Mater.* (2024) 2314247, <https://doi.org/10.1002/ADMA.202314247>.
- [22] M. Wang, C. Jiang, S. Zhang, X. Song, Y. Tang, H.M. Cheng, Reversible calcium alloying enables a practical room-temperature rechargeable calcium-ion battery with a high discharge voltage, *Nat. Chem.* (10) (2018) 667–672, <https://doi.org/10.1038/s41557-018-0045-4>, 2018 106.
- [23] S. Guan, J. Zhou, S. Sun, Q. Peng, X. Guo, B. Liu, X. Zhou, Y. Tang, Nonmetallic Se/N Co-doped amorphous carbon anode collaborates to realize ultra-high capacity and fast potassium storage for potassium dual-ion batteries, *Adv. Funct. Mater.* (2024) 2314890, <https://doi.org/10.1002/ADFM.202314890>.
- [24] T. Zhang, J. Li, R. Bi, J. Song, L. Du, T. Li, H. Zhang, Q. Guo, J. Luo, One-step microwave synthesis of in situ grown NiTe nanosheets for solid-state asymmetric supercapacitors and oxygen evolution reaction, *J. Alloys Compd.* 909 (2022) 164786, <https://doi.org/10.1016/J.JALLCOM.2022.164786>.
- [25] T. Ahmad, B.M. Alotaibi, A.W. Alrowaily, H.A. Alyousef, M.F. Alotiby, M. Abdullah, A. Dahshan, A.M.A. Henaish, S. Aman, Hydrothermal fabrication of highly effective g-C<sub>3</sub>N<sub>4</sub>/NiIn<sub>2</sub>S<sub>2</sub> composite as supercapacitor electrode material, *Ceram. Int.* (2024), <https://doi.org/10.1016/J.CERAMINT.2024.01.429>.
- [26] J. Cherussery, N. Choudhary, K. Sambath Kumar, Y. Jung, J. Thomas, Recent trends in transition metal dichalcogenide based supercapacitor electrodes, *Nanoscale Horizons* 4 (2019) 840–858, <https://doi.org/10.1039/C9NH00152B>.
- [27] Y. Zhao, J. Jing, L. Chen, F. Xu, H. Hou, Current Research Status of Interface of Ceramic-Metal Laminated Composite Material for Armor Protection, *Jinshu Xueba/Acta Metallurgica Sinica* 57 (2021) 1107–1125, <https://doi.org/10.11900/0412.1961.2021.00051>.
- [28] M. Abdullah, M.Z. Ansari, Z. Ahamed, P. John, S. Manzoor, A.M. Shawky, H. H. Hegazy, A.H. Chughtai, M.N. Ashiq, T.A. Taha, Ag<sub>2</sub>Se/SnTe nanorod as potential candidate for energy conversion system developed via hydrothermal route, *Ceram. Int.* 49 (2023) 6780–6789, <https://doi.org/10.1016/J.CERAMINT.2022.10.131>.
- [29] B. Ye, X. Cao, Q. Zhao, J. Wang, Coelectrodeposition of NiSe/ZnSe hybrid nanostructures as a battery-type electrode for an asymmetric supercapacitor, *J. Phys. Chem. C* 124 (2020) 21242–21249, [https://doi.org/10.1021/ACS.JPCC.0C05125.SI\\_001.PDF](https://doi.org/10.1021/ACS.JPCC.0C05125.SI_001.PDF).
- [30] J. Liu, L. Ren, J. Luo, J. Song, Microwave synthesis of NiSe/NiTe<sub>2</sub> nanocomposite grown in situ on Ni foam for all-solid-state asymmetric supercapacitors, *Colloids Surfaces A Physicochem. Eng. Asp.* 647 (2022) 129093, <https://doi.org/10.1016/J.COLSURFA.2022.129093>.
- [31] N. Xue, W. Li, L. Shao, Z. Tu, Y. Chen, S. Dai, L. Zhu, Comparison of Cold-Sprayed Coatings of Copper-Based Composite Deposited on AZ31B Magnesium Alloy and 6061 T6 Aluminum Alloy Substrates, *Materials* 16 (14) (2023) 5120, <https://doi.org/10.3390/ma16145120>.
- [32] A.P. Alegaonkar, M.A. Mahadalkar, P.S. Alegaonkar, B.B. Kale, S.K. Pardeshi, High performance tellurium-reduced graphene oxide pseudocapacitor electrodes, *Electrochim. Acta* 291 (2018) 225–233, <https://doi.org/10.1016/J.ELECTACTA.2018.09.116>.
- [33] M.S. Vidhya, R. Yuvakkumar, P.S. Kumar, G. Ravi, D. Velauthapillai, P.N. Asrami, Electrochemical enhancement of binary CuSe<sub>2</sub>@MoSe<sub>2</sub> composite nanorods for supercapacitor application, *Top. Catal.* 65 (2022) 668–676, <https://doi.org/10.1007/S11244-021-01508-Y/FIGURES/8>.
- [34] M. Hussain, M.M. Alanazi, S.A.M. Abdelmohsen, S.D. Alahmari, M. Abdullah, S. Aman, A.G. Al-Sehemi, A.M.A. Henaish, Z. Ahmad, H.M.T. Farid, Enhanced performance of hydrothermally prepared Ag<sub>2</sub>Se/rGO nanosheet composite for energy storage applications, *Diam. Relat. Mater.* 142 (2024) 110764, <https://doi.org/10.1016/J.DIAMOND.2023.110764>.
- [35] S. Yang, Z. Huang, Q. Hu, Y. Zhang, F. Wang, H. Wang, Y. Shu, Proportional Optimization Model of Multiscale Spherical BN for Enhancing Thermal Conductivity, *ACS Applied Electronic Materials* 4 (9) (2022) 4659–4667, <https://doi.org/10.1021/acsealm.2c00878>.
- [36] M. Hussain, M.M. Alanazi, S.A.M. Abdelmohsen, S.D. Alahmari, M. Abdullah, S. Aman, A. Dahshan, A.M.A. Henaish, Z. Ahmad, H.M.T. Farid, Hydrothermal synthesis of Nd-doped FeTiO<sub>3</sub> perovskite electrode for enhanced energy storage applications, *J. Energy Storage* 84 (2024) 110920, <https://doi.org/10.1016/J.JEST.2024.110920>.
- [37] K.A. Geelani, B.M. Alotaibi, A.W. Alrowaily, H.A. Alyousef, M.F. Alotiby, M. Abdullah, A. Dahshan, Fabrication of Mn doped BiFeO<sub>3</sub> as an electrode material for supercapacitor applications, *J. Energy Storage* 85 (2024) 111054, <https://doi.org/10.1016/J.JEST.2024.111054>.
- [38] M. Abdullah, P. John, K. Jabbour, M.I. Ahmad, S. Khan, M.S. Waheed, M. D. Albaqami, M. Sheikh, M.F. Ehsan, M.N. Ashiq, Improvement in capacitive performance of ZnS with MnO<sub>2</sub> via composite (ZnS/MnO<sub>2</sub>) strategy developed by hydrothermal technique, *J. Energy Storage* 78 (2024) 110034, <https://doi.org/10.1016/J.JEST.2023.110034>.
- [39] B. Pandit, S.A. Pande, B.R. Sankapal, Facile SILAR processed Bi<sub>2</sub>ZS<sub>3</sub>PbS solid solution on MWCNTs for high-performance electrochemical supercapacitor, *Chin. J. Chem.* 37 (2019) 1279–1286, <https://doi.org/10.1002/CJOC.201900222>.
- [40] M. Ali, S.D. Alahmari, S.A.M. Abdelmohsen, M.M. Alanazi, A.G. Al-Sehemi, M. Abdullah, S. Aman, H.M.T. Farid, Fabrication of MnSe/WSe<sub>2</sub> nanohybrid electrode prepared through hydrothermal method for supercapacitor applications, *Ceram. Int.* 50 (2024) 6931–6940, <https://doi.org/10.1016/J.CERAMINT.2023.12.042>.

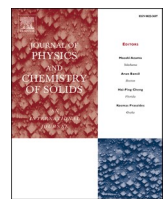
- [41] H. Zhang, W. Zhou, X. Li, J. Xu, Y. Shi, B. Wang, F. Miao, High temperature Raman investigation of few-layer MoTe<sub>2</sub>, *Appl. Phys. Lett.* 108 (2016), <https://doi.org/10.1063/1.4943139/31791>.
- [42] Y. Sun, Y. Wang, D. Sun, B.R. Carvalho, C.G. Read, C. Lee, Z. Lin, K. Fujisawa, J. A. Robinson, V.H. Crespi, M. Terrones, R.E. Schaak, Low-Temperature solution synthesis of few-layer 1T'-MoTe<sub>2</sub> nanostructures exhibiting lattice compression, *Angew. Chem.* 128 (2016) 2880–2884, <https://doi.org/10.1002/ANGE.201510029>.
- [43] M. Zeshan, F.F. Alharbi, S.D. Alahmari, M. Abdullah, A.G. Al-Sehemi, A.M. A. Henaish, Z. Ahmad, M.S. Waheed, S. Aman, H.M.T. Farid, Fabrication of niobium selenide-based rGO hybrid nanoparticles by hydrothermal method for supercapacitor applications, *Ceram. Int.* 50 (2024) 7110–7120, <https://doi.org/10.1016/J.CERAMINT.2023.12.075>.
- [44] M. Abdullah, S.D. Alahmari, S. Aman, S.R. Ejaz, Y.A. Haleem, S. Gouadria, A.G. Al-Sehemi, A.M.A. Henaish, Z. Ahmad, H.M.T. Farid, Facile fabrication of AgFeS<sub>2</sub> nanostructure via hydrothermal route for supercapacitor application, *J. Energy Storage* 77 (2024) 109875, <https://doi.org/10.1016/J.JEST.2023.109875>.
- [45] M.S. Vidhya, R. Yuvakkumar, P.S. Kumar, G. Ravi, D. Velauthapillai, P.N. Asrami, Electrochemical enhancement of binary CuSe<sub>2</sub>@MoSe<sub>2</sub> composite nanorods for supercapacitor application, *Top. Catal.* 65 (2022) 668–676, <https://doi.org/10.1007/S11244-021-01508-Y/METRICS>.
- [46] M. Li, J. Ding, T. Wu, W. Zhang, Iron-Doped monoclinic strontium iridate as a highly efficient oxygen evolution electrocatalyst in acidic media, *Nanomaterials* 13 (2023) 797, <https://doi.org/10.3390/NANO13050797/S1>.
- [47] A.I. Abdel-Salam, S.Y. Attia, F.I. El-Hosiny, M.A. Sadek, S.G. Mohamed, M. M. Rashad, Facile one-step hydrothermal method for NiCo<sub>2</sub>S<sub>4</sub>/rGO nanocomposite synthesis for efficient hybrid supercapacitor electrodes, *Mater. Chem. Phys.* 277 (2022) 125554, <https://doi.org/10.1016/J.MATCHEMPHYS.2021.125554>.
- [48] D.A. Alshammari, I.A. Ahmad, S.D. Alahmari, M. Abdullah, S. Aman, N. Ahmad, A. M.A. Henaish, Z. Ahmad, H.M.T. Farid, Z.M. El-Bahy, Electrochemical investigation of niobium doped nickel selenide nanostructure for supercapacitor devices, *J. Energy Storage* 75 (2024) 109886, <https://doi.org/10.1016/J.JEST.2023.109886>.
- [49] D.D. Farashah, F. Beigloo, A.M. Zardkhoshouei, S.S. Hosseiny Davarani, Unveiling the potential of nanosheet-based NiTe<sub>2</sub>@MnTe hollow nanospheres in hybrid supercapacitor technology, *Sustain. Energy Fuels* 7 (2023) 4922–4934, <https://doi.org/10.1039/D3SE00919J>.
- [50] L. Wan, T. Jiang, Y. Zhang, J. Chen, M. Xie, C. Du, 1D-on-1D core–shell cobalt iron selenide @ cobalt nickel carbonate hydroxide hybrid nanowire arrays as advanced battery-type supercapacitor electrode, *J. Colloid Interface Sci.* 621 (2022) 149–159, <https://doi.org/10.1016/J.JCIS.2022.04.072>.
- [51] L.A. El Maati, R.Y. Khosa, S.D. Alahmari, F.F. Alharbi, M. Abdullah, S. Aman, A. G. Al-Sehemi, A.M.A. Henaish, Z. Ahmad, H.M.T. Farid, Facile synthesis of environmental friendly Sm<sub>2</sub>O<sub>3</sub>/rGO electrode as an alternative source for energy storage devices, *Diam. Relat. Mater.* 142 (2024) 110769, <https://doi.org/10.1016/J.JDIAMOND.2023.110769>.
- [52] H.P. Karki, H. Kim, J. Jung, J. Oh, Synthesis of molybdenum sulfide/tellurium hetero-composite by a simple one-pot hydrothermal technique for high-performance supercapacitor electrode material, *Nanomaterials* 11 (2021) 2346, <https://doi.org/10.3390/NANO11092346/S1>.
- [53] K.S. Bhat, S. Shenoy, H.S. Nagaraja, K. Sridharan, Porous cobalt chalcogenide nanostructures as high performance pseudo-capacitor electrodes, *Electrochim. Acta* 248 (2017) 188–196, <https://doi.org/10.1016/J.ELECTACTA.2017.07.137>.
- [54] M. Abdullah, P. John, K.F. Fawy, S. Manzoor, K.Y. Butt, A.G. Abid, M. Messali, M. Najam-Ul-Haq, M.N. Ashiq, Facile synthesis of the SnTe/SnSe binary nanocomposite via a hydrothermal route for flexible solid-state supercapacitors, *RSC Adv.* 13 (2023) 12009–12022, <https://doi.org/10.1039/D3RA01028G>.
- [55] S. Ullah, G. Yasin, A. Ahmad, L. Qin, Q. Yuan, A.U. Khan, U.A. Khan, A.U. Rahman, Y. Slimani, Construction of well-designed 1D selenium–tellurium nanorods anchored on graphene sheets as a high storage capacity anode material for lithium-ion batteries, *Inorg. Chem. Front.* 7 (2020) 1750–1761, <https://doi.org/10.1039/C9QI01701A>.
- [56] S.J. Patil, A.C. Lokhande, D.W. Lee, J.H. Kim, C.D. Lokhande, Chemical synthesis and supercapacitive properties of lanthanum telluride thin film, *J. Colloid Interface Sci.* 490 (2017) 147–153, <https://doi.org/10.1016/J.JCIS.2016.11.020>.
- [57] M.S.U. Shah, X. Zuo, M.Z.U. Shah, H. Hou, M.K. Shah, I. Ahmad, M. Sajjad, A. Shah, Nickel selenide nano-cubes anchored on cadmium selenide nanoparticles: first-ever designed as electrode material for advanced hybrid energy storage applications, *J. Energy Storage* 63 (2023) 107065, <https://doi.org/10.1016/J.JEST.2023.107065>.
- [58] B. Pandit, C.D. Jadhav, P.G. Chavan, H.S. Tarkas, J.V. Sali, R.B. Gupta, B. R. Sankapal, Two-dimensional hexagonal SnSe nanosheets as binder-free electrode material for high-performance supercapacitors, *IEEE Trans. Power Electron.* 35 (2020) 11344–11351, <https://doi.org/10.1109/TPEL.2020.2989097>.
- [59] M. Abdullah, N. Alwadai, M. Al Huwayz, S. Manzoor, P. John, A.G. Abid, M. I. Ghouri, S. Aman, M.S. Al-Buraihi, M.N. Ashiq, Effect of Ag content on the electrochemical performance of Ag<sub>2</sub>Te nanostructures synthesized by hydrothermal route for supercapacitor applications, *Energy Fuel.* 37 (2023) 1297–1309, [https://doi.org/10.1021/ACS.ENERGYFUELS.2C03279/ASSET/IMAGES/MEDIUM/EF2C03279\\_0012.GIF](https://doi.org/10.1021/ACS.ENERGYFUELS.2C03279/ASSET/IMAGES/MEDIUM/EF2C03279_0012.GIF).
- [60] T. Zahra, M.M. Alanazi, S.D. Alahmari, S.A.M. Abdelmohsen, M. Abdullah, S. Aman, A.G. Al-Sehemi, A.M.A. Henaish, Z. Ahmad, H.M. Tahir Farid, Hydrothermally synthesized ZnSe@FeSe nanocomposite: a promising candidate for energy storage devices, *Int. J. Hydrogen Energy* 59 (2024) 97–106, <https://doi.org/10.1016/J.IJHYDENE.2024.01.293>.
- [61] D. Ni, Y. Chen, X. Yang, C. Liu, K. Cai, Microwave-assisted synthesis method for rapid synthesis of tin selenide electrode material for supercapacitors, *J. Alloys Compd.* 737 (2018) 623–629, <https://doi.org/10.1016/J.JALCOM.2017.12.037>.
- [62] Y. Tian, Y. Ruan, J. Zhang, Z. Yang, J. Jiang, C. Wang, Controllable growth of NiSe nanorod arrays via one-pot hydrothermal method for high areal-capacitance supercapacitors, *Electrochim. Acta* 250 (2017) 327–334, <https://doi.org/10.1016/J.ELECTACTA.2017.08.084>.
- [63] X. Xu, L. Pei, Y. Yang, J. Shen, M. Ye, Facile synthesis of NiWO<sub>4</sub>/reduced graphene oxide nanocomposite with excellent capacitive performance for supercapacitors, *J. Alloys Compd.* 654 (2016) 23–31, <https://doi.org/10.1016/J.JALCOM.2015.09.108>.
- [64] A. Vazhayil, J. Thomas, N. Thomas, Cobalt doping in LaMnO<sub>3</sub> perovskite catalysts – B site optimization by solution combustion for oxygen evolution reaction, *J. Electroanal. Chem.* 918 (2022) 116426, <https://doi.org/10.1016/J.JELECHEM.2022.116426>.
- [65] S.A. Pande, B. Pandit, B.R. Sankapal, Vanadium oxide anchored MWCNTs nanostructure for superior symmetric electrochemical supercapacitors, *Mater. Des.* 182 (2019) 107972, <https://doi.org/10.1016/J.MATDES.2019.107972>.
- [66] B. Pandit, N. Kumar, P.M. Koinkar, B.R. Sankapal, Solution processed nanostructured cerium oxide electrode: electrochemical engineering towards solid-state symmetric supercapacitor device, *J. Electroanal. Chem.* 839 (2019) 96–107, <https://doi.org/10.1016/J.JELECHEM.2019.02.047>.

## Update

**Journal of Physics and Chemistry of Solids**

Volume 194, Issue , November 2024, Page

DOI: <https://doi.org/10.1016/j.jpcs.2024.112258>



## Corrigendum to “Facile synthesis of SnSe–MnTe nanocomposite as a promising electrode for supercapacitor applications” [J. Phys. Chem. Solid. 192 (September 2024) 112058]



Abdul Khaliq <sup>a,\*</sup>, Meznah M. Alanazi <sup>b</sup>, Shaimaa A.M. Abdelmohsen <sup>b</sup>, Saeed D. Alahmari <sup>c</sup>, Khalid I. Hussein <sup>d</sup>, A.M.A. Henaish <sup>e,f</sup>, Muhammad Abdullah <sup>g</sup>

<sup>a</sup> Institute of Physics, Gomal University, Dera Ismail Khan, KPK, Pakistan

<sup>b</sup> Department of Physics, College of Science, Princess Nourah bint Abdulrahman University, P.O. Box 84428, Riyadh, 11671, Saudi Arabia

<sup>c</sup> Department of Chemistry, Faculty of Science, Jazan University, P.O. Box 2097, 45142, Jazan, Saudi Arabia

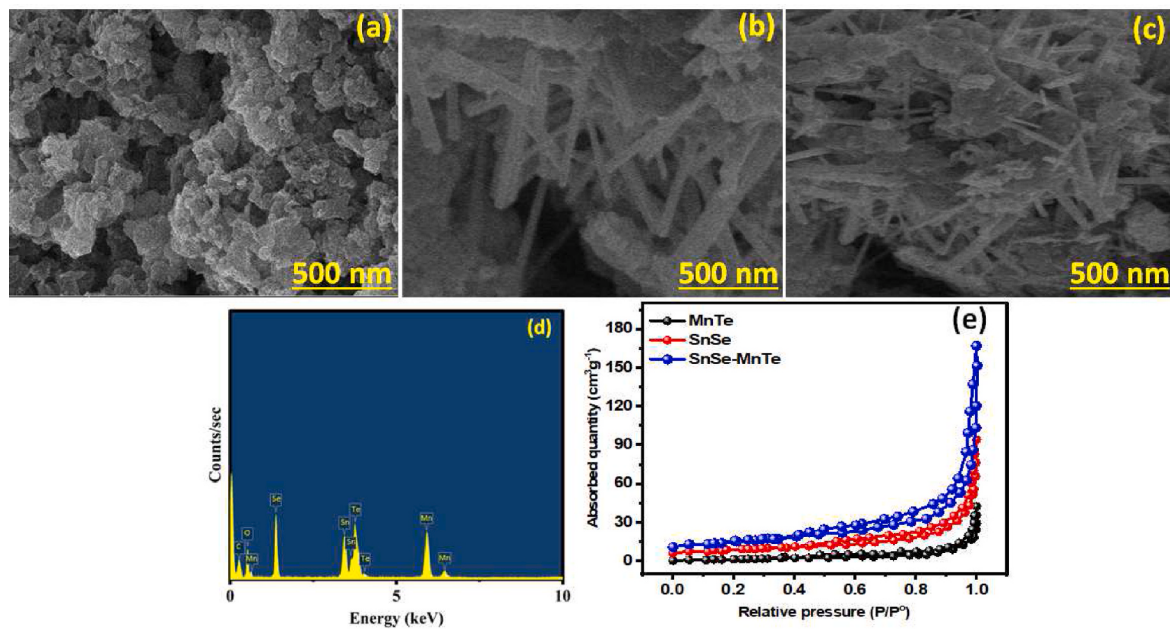
<sup>d</sup> Department of Radiological Sciences, College of Applied Medical Sciences, King Khalid University, Abha, 61421, Saudi Arabia

<sup>e</sup> Physics Department, Faculty of Science, Tanta University, Tanta, 31527, Egypt

<sup>f</sup> NANOTECH Center, Ural Federal University, Ekaterinburg, 620002, Russia

<sup>g</sup> Department of Chemistry, Government College University Lahore, Lahore, 54000, Pakistan

Fig. 2 (d).



DOI of original article: <https://doi.org/10.1016/j.jpcs.2024.112058>.

\* Corresponding author.

E-mail address: [abdulkhaliq78965@gmail.com](mailto:abdulkhaliq78965@gmail.com) (A. Khaliq).

<https://doi.org/10.1016/j.jpcs.2024.112258>

Available online 15 August 2024

0022-3697/© 2024 Elsevier Ltd. All rights are reserved, including those for text and data mining, AI training, and similar technologies.

<The authors regret that labeling in Fig. 2 (d) was wrong. It will be cleared for the readers through corrigendum. We really apologize for

this mistake.>.

The authors would like to apologize for any inconvenience caused.